Article

Pyrogenic Iron(III)-Doped TiO Nanopowders Synthesized in RF Thermal Plasma: Phase Formation, Defect Structure, Band Gap, and Magnetic Properties

X. H. Wang, J.-G. Li, H. Kamiyama, M. Katada, N. Ohashi, Y. Moriyoshi, and T. Ishigaki

J. Am. Chem. Soc., **2005**, 127 (31), 10982-10990• DOI: 10.1021/ja051240n • Publication Date (Web): 15 July 2005

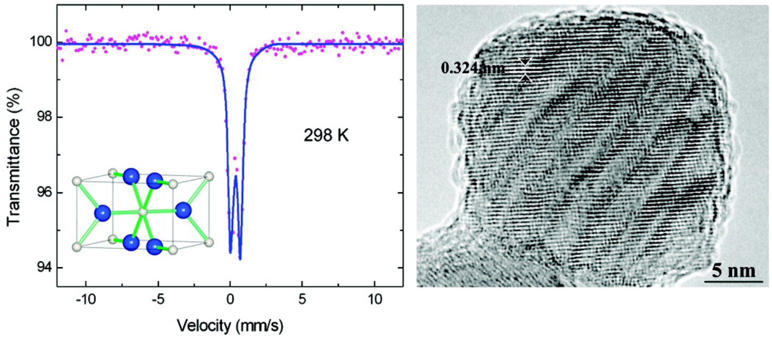

Journal of the American Chemical Society is published by the American Chemical Society. 1155 Sixteenth Street N.W., Washington, DC 20036

J|A|C|S

ARTICLES

Pyrogenic Iron(III)-Doped TiO_2 Nanopowders Synthesized in RF Thermal Plasma: Phase Formation, Defect Structure, Band Gap, and Magnetic Properties

X. H. Wang,[†] J.-G. Li,[†] H. Kamiyama,[†,‡] M. Katada,[§] N. Ohashi,[†] Y. Moriyoshi,[‡] and T. Ishigaki*,[†]

Contribution from the Advanced Materials Laboratory, National Institute for Materials Science, 1-1 Namiki, Tsukuba, Ibaraki 305-0044, Japan, Department of Materials Chemistry, Hosei University, Kajino-cho, Koganei-shi, Tokyo 184-8584, Japan, and Graduate School of Science, Tokyo Metropolitan University, Minami-ohsawa, Hachioji, Tokyo 192-0397, Japan

Received February 27, 2005; E-mail: ISHIGAKI.Takamasa@nims.go.jp

Abstract: Iron(III)-doped TiO_2 nanopowders, with controlled iron to titanium atomic ratios ($R_{Fe/Ti}$) ranging from nominal 0 to 20%, were synthesized using oxidative pyrolysis of liquid-feed metallorganic precursors in a radiation-frequency (RF) thermal plasma. The valence of iron doped in the TiO_2, phase formation, defect structures, band gaps, and magnetic properties of the resultant nanopowders were systematically investigated using Mössbauer spectroscopy, XRD, Raman spectroscopy, TEM/HRTEM, UV−vis spectroscopy, and measurements of magnetic properties. The iron doped in TiO_2 was trivalent (3+) in a high-spin state as determined by the isomer shift and quadrupole splitting from the Mössbauer spectra. No other phases except anatase and rutile TiO_2 were identified in the resultant nanopowders. Interestingly, thermodynamically metastable anatase predominated in the undoped TiO_2 nanopowders, which can be explained from a kinetic point of view based on classical homogeneous nucleation theory. With iron doping, the formation of rutile was strongly promoted because rutile is more tolerant than anatase to the defects such as oxygen vacancies resulting from the substitution of Fe^{3+} for Ti^{4+} in TiO_2. The concentration of oxygen vacancies reached a maximum at $R_{Fe/Ti} = 2\%$ above which excessive oxygen vacancies tended to concentrate. As a result of this concentration, an extended defect like crystallographic shear (CS) structure was established. With iron doping, red shift of the absorption edges occurred in addition to the d−d electron transition of iron in the visible light region. The as-prepared iron-doped TiO_2 nanopowders were paramagnetic in nature at room temperature.

Introduction

Titanium dioxide is used in heterogeneous catalysis, as a photocatalyst, in solar cells for the production of hydrogen and electric energy, as a gas sensor, as a white pigment (e.g., in paints and cosmetic products), as a corrosion-protective coating, as an optical coating, in ceramics, and in electric devices such as varistors.[1]

As a widely used heterogeneous catalyst, TiO_2 has been extensively studied in the field of surface science. Current research on TiO_2 is focused on its photoelectric and photochemical properties. The initial work by Fujishima and Honda[2] on the splitting of water into H_2 and O_2 on TiO_2 electrodes under UV irradiation stimulated much of the early works on TiO_2.[3] Unfortunately, the quantum yield of TiO_2 is too low for photochemical conversion of solar energy. The use of colloidal suspensions with the addition of dye molecules significantly improved the efficiency of solar cells.[4] Most of the applied research on titania relates to its use as heterogeneous photocatalysis for environmental applications.[5] The photocatalytic activity of titania originates from the production of excited electrons (e^-) in the conduction band, along with corresponding positive holes (h^+) in the valence band through the absorption of suitable illumination. The energetically excited charge carriers are mobile and capable of initiating numerous chemical reactions, usually via the production of radical species on the titania surface. However, these charge carriers are unstable and can recombine rapidly, dissipating the absorbed energy as heat. Consequently, the photocatalytic efficiency depends on competition between the two processes, viz., the ratio of the surface charge-carrier transfer rate to the electron−hole recombination rate. To improve the photocatalytic efficiency of TiO_2-based photocatalysis, the e^-−h^+ recombination rate must be reduced. Doping TiO_2 with transition metal ions has been shown to be

---

[†] National Institute for Materials Science.

[‡] Hosei University.

[§] Tokyo Metropolitan University.

(1) Diebold, U. *Surf. Sci. Rep.* **2003**, *48*, 53−229.

(2) Fujishima, A.; Honda, K. *Nature* **1972**, *238*, 37.

(3) (a) Henrich, V. E.; Dresselhaus, G.; Zeiger, H. J. *Phys. Rev. Lett.* **1976**, *36*, 1335−1339. (b) Lo, W. J.; Chung, Y. W.; Somorjai, G. A. *Surf. Sci.* **1978**, *71*, 199−219.

(4) O'Regan, B.; Gratzel, M. *Nature* **1991**, *353*, 737−740.

(5) Hoffmann, M. R.; Martin, S. T.; Choi, W. Y.; Bahnemann, D. W. *Chem. Rev.* **1995**, *95*, 69−96.

10.1021/ja051240n CCC: $30.25

an effective method of enhancing the photocatalytic efficiency in some heterogeneous photocatalysis systems.[5]

More recently, the field of spintronics has developed rapidly because of the increasing demand by the information technology industry for faster data processing and larger charge storage capacity.[6] The use of metal-ferromegnetic-semiconductor based heterostructures for this purpose has been extensively studied. However, it is difficult to transfer electron spin across the ferromagnetic-semiconductor interfaces mainly due to their dissimilar electronic conductivities.[7] Another promising approach is to integrate ferromagnetic semiconductors with existing semiconductors.[8] Room-temperature ferromagnetism (RTF) properties were reported in Co-doped TiO_2 thin films prepared using methods of pulsed laser deposition,[9] oxygen plasma assisted molecular beam epitaxy,[10] reactive cosputtering,[11] and liquid delivery metallorganic vapor deposition.[12] In contrast, Co-doped TiO_2 thin films prepared using several techniques such as spray pyrolysis[13] were found to be paramagnetic rather than ferromagnetic at room temperature. The divergence between the films prepared using the different techniques raises speculation about the origin of RTF of these films. Matsumoto et al.[9] commented that magnetic Co clusters precipitated in TiO_2 matrix might be responsible for the observed RTF, but no evidence for Co clusters was found using XRD and TEM. This possibility was also raised by several other researchers, who found evidence for the presence of Co clusters from magnetic study.[14] Since magnetic elements of Co and Fe have similar electronic configurations, a study of the magnetic property of Fe-doped TiO_2 might be helpful in understanding the origin of RTF in Co-doped TiO_2 thin films and/or powders.

Iron-doped TiO_2 has been synthesized using wet chemical routes.[15,16] Conventional methods of synthesis require either postannealing to obtain crystallized samples or the Fe/Ti molar ratios in the resultant powders deviated notably from those of the precursor.[15] However, the postannealing resulted in phase segregation for samples with an iron content of more than 3 at. % or 5 wt %.[16] RF thermal plasma is characterized by extremely high temperatures (3000−10 000 K) and rapid heating and cooling rates (~10^6 K/s), making it particularly suitable for synthesizing lightly and highly doped oxides nanopowders with good crystallinity and homogeneous dopant distribution in a very short time. In this work, we fabricated iron(III)-doped nanopowders with controlled $R_{Fe/Ti}$ ranging from nominal 0 to 20% under extreme synthesis conditions using RF thermal plasma as a reaction zone. The effects of the iron-dopant concentration on the phase formation, defect structure, band gap, and magnetic properties of the resultant powders were systematically investigated.

Experimental Section

Preparation of Materials. Pyrogenic TiO_2 was prepared by plasma-assisted oxidative pyrolysis using reagent-grade titanium tetraisobutoxide (TTIB, 97%, Kanto Kagaku, Tokyo, Japan) and ferrocene (98%, Kanto Kagaku, Tokyo, Japan) as precursors. The hydrolysis of the TTIB was restrained through a chelation reaction with diethanolamine (DEA, 99%, Kanto Kagaku, Tokyo, Japan). Equimolar TTIB and DEA were first admixed in a beaker. Preweighed ferrocene dissolved in ethanol (99.5%, Wako Pure Chemical Industies, Ltd., Osaka, Japan) was then added under continuous stirring until a homogeneous solution precursor was obtained. In all experiments, the titanium concentration was kept constant (1.5 mol/L) by adding ethanol. The atomic ratios of Fe to Ti in the precursors, hereafter referred to as $R_{Fe/Ti}$, were selected: nominal 0, 0.05, 0.5, 1, 2, 3, 5, 10, and 20%. The precursors, stored in beakers covered with moisture-resistant films, showed no changes in color and/or transparency even after 2 months of storage.

Synthesis of TiO_2 nanopowders was carried out in a RF thermal plasma assisted aerosol reactor. The plasma was generated by a PL-50 induction plasma torch (TEKNA Plasma Systems, Sherbrooke, QC, Canada) connected to a 2 MHz RF power-supply system (Nihon Koshuha Co. Ltd., Yokohama, Japan) operated at 25 kW. In the oxidative pyrolysis, liquid precursor was fed through a water-cooled atomizer probe into the plasma at a rate of 3.6 mL/min. An argon flow (5 L/min) was used to atomize the liquid leaving the probe tip. Argon (30 L/min) was injected as the central gas, and a mixture of $Ar-O_2$ (Ar, 20 L/min; O_2, 70 L/min) was as the sheath gas. The chamber pressure was maintained at 66.7 kPa with the aid of an automatically adjustable vacuum pump system. A schematic illustration of the configuration of the apparatus is available in the literature.[17]

Characterizations. For chemical analyses by inductively coupled plasma-atomic emission spectroscopy (ICP-AES, SPS1700HVR, Seiko Instruments Inc., Chiba, Japan), the as-prepared powders were dissolved in $K_2S_2O_7$ and diluted sulfuric acid. The measurement wavelengths for Ti and Fe are 308.802 and 238.204 nm, respectively. The ^{57}Fe Mössbauer spectra were obtained using a Wissel Mössbauer spectrometer with a proportional counter. A ^{57}Co(Rh) source moving in a constant acceleration mode was used for the measurements. The velocity scale was calibrated by using a metallic iron-foil spectrum. The isomer shift and quadrupole splitting were obtained by least-squares fitting of the data to Lorentzian line shapes. The isomer shift values were reported relative to metallic iron at room temperature. The X-ray diffraction (XRD, RINT 2200/PC, Rigaku, Akishima, Tokyo, Japan) patterns were recorded using Cu Kα radiation with a tube voltage of 40 mV and current of 40 mA. Scans were stepwise from 15° to 100° with a step of 0.02° (2θ) and a dwelling time of 6 s. Two methods were used to determine the quantitative phase compositions from XRD data, namely, Chung's method[18] and the Rietveld method using a RIETAN-2000 software.[19] For transmission electron microscopy/high-resolution trans-

---

(6) (a) Jedema, F. J.; Filip, A. T.; van Wees, B. J. *Nature* **2001**, *410*, 345−348. (b) Salis, G.; Kato, K.; Ensslin, K.; Driscoll, D. C.; Gossard, A. C.; Awschalom, D. D. *Nature* **2001**, *414*, 619−622.

(7) (a) Hammar, P. R.; Bennett, B. R.; Yang, M. J.; Johnson, M. *Phys. Rev. Lett.* **1999**, *83*, 203−206. (b) Bland, J. A. C.; Hirohata, A.; Guertler, C. M.; Xu, Y. B.; Tselepi, M. *J. Appl. Phys.* **2001**, *89*, 6740−6744. (c) Schmidt, G.; Molenkamp, L. W. *J. Appl. Phys.* **2001**, *89*, 7443−7447. (d) Young, D. K.; Johnston-Halperin, E.; Awschalom, D. D.; Ohno, Y.; Ohno, H. *Appl. Phys. Lett.* **2002**, *80*, 1598−1600.

(8) (a) Ohno, H.; Shen, A.; Matsukura, F.; Oiwa, A.; Endo, A.; Katsumoto, S.; Iye, Y. *Appl. Phys. Lett.* **1996**, *69*, 363−365. (b) Kronik, L.; Jian, M.; Chelikowsky, J. R. *Phy. Rev. B* **2002**, *66*, 041203.

(9) Matsumoto, Y.; Murakami, M.; Shono, T.; Hasegawa, T.; Fukumura, T.; Kawasaki, M.; Ahmet, P.; Chikyow, T.; Koshihara, S.; Koinuma, H. *Science* **2001**, *291*, 854−856.

(10) Chambers, S. A.; Thevuthasan, S.; Farrow, R. F. C.; Marks, R. F.; Thiele, J. U.; Folks, L.; Samant, M. G.; Kellock, A. J.; Ruzycki, N.; Ederer, D. L.; Diebold, U. *Appl. Phys. Lett.* **2001**, *79*, 3467−3469.

(11) (a) Park, W. K.; Ortega-Hertogs, R. J.; Moodera, J. S.; Punnoose, A.; Seehra, M. S. *J. Appl. Phys.* **2002**, *91*, 8093−8095. (b) Punnoose, A.; Seehra, M. S.; Park, W. K.; Moodera, J. S. *J. Appl. Phys.* **2003**, *93*, 7867−7869.

(12) Seong, N. J.; Yoon, S. G.; Cho, C. R. *Appl. Phys. Lett.* **2002**, *81*, 4209−4211.

(13) Manivannan, A.; Seehra, M. S.; Majumder, S. B.; Katiyar, R. S. *Appl. Phys. Lett.* **2003**, *83*, 111−113.

(14) Kim, D. H.; Yang, J. S.; Lee, K. W.; Bu, S. D.; Kim, D. W.; Noh, T. W.; Oh, S. J.; Kim, Y. W.; Chang, J. S.; Tanaka, H.; Lee, H. Y.; Kawai, T.; Won, J. Y.; Park, S. H.; Lee, J. C. *J. Appl. Phys.* **2003**, *93*, 6125−6132.

(15) Hirano, M.; Joji, T.; Inagaki, M. *J. Am. Ceram. Soc.* **2004**, *87*, 35−41.

(16) (a) Zhang, Y. H.; Reller, A. *J. Mater. Chem.* **2001**, *11*, 2537−2541. (b) Wang, J. A.; Limas-Ballesteros, R.; Lopez, T.; Moreno, A.; Gomez, R.; Novaro, O.; Bokhimi, X. *J. Phys. Chem. B* **2001**, *105*, 9692−9698. (c) Perkas, N.; Palchik, O.; Brukental, I.; Nowik, I.; Gofer, Y.; Koltypin, Y.; Gedanken, A. *J. Phys. Chem. B* **2003**, *107*, 8772−8778. (d) Zhang, Y. H.; Ebbinghaus, S. G.; Weidenkaff, A.; Kurz, T.; von Nidda, H. A. K.; Klar, P. J.; Gungerich, M.; Reller A. *Chem. Mater.* **2003**, *15*, 4028−4033.

(17) Li, Y. L.; Ishigaki, T. *Chem. Mater.* **2001**, *13*, 1577−1584.

(18) Chung, F. H. *J. Appl. Crystallogr.* **1974**, *7*, 526−531.

(19) Izumi, F.; Ikeda, T. *Mater. Sci. Forum* **2000**, *321−3*, 198−203.

Table 1. Chemical Analysis Results of As-Prepared Nanopowders

precursor	synthesized powder			
Fe/Ti[a] (%)	Ti (wt %)	Fe (wt %)	Fe/Ti[a] (%)	Fe/(Fe + Ti)[a] (%)
0.0	60.4	0.006	0.0085	0.0085
0.05	59.8	0.036	0.052	0.052
0.50	59.0	0.30	0.44	0.44
1.0	59.7	0.64	0.92	0.91
2.0	58.7	1.29	1.88	1.84
3.0	58.0	1.93	2.85	2.77
5.0	56.6	2.94	4.45	4.26
10.0	53.5	5.92	9.48	8.66
20.0	48.4	11.1	19.7	16.4

[a] Atomic ratios.

mission electron microscopy (TEM/HRTEM, JEM-2000EX, JEOL, Akishima, Tokyo, Japan) analyses, a drop of the nanopowders suspended in ethanol was put on an amorphous carbon-coated copper grid and dried naturally. The Raman spectra were recorded in an NR-1800 laser Raman spectrometer (JASCO, Hachioji, Tokyo, Japan) using an Ar^+ laser with a wavelength of 514.53 nm. The power output was 50 mW. The diffuse reflectance UV−vis spectra were collected by a V-570 UV/VIS/NIR spectrophotometer (JASCO, Hachioji, Tokyo, Japan) with $BaSO_4$ as a reference. The as-prepared nanopowders were pressed into cylinders, and their magnetic properties were then measured at room temperature using a Lakeshore 735 vibrating sample magnetometer (Lake Shore Cryotronics, Inc., Westerville, OH).

Results

Chemical Analysis. The results of quantitative elemental analysis by ICP-AES indicated that the Fe/Ti atomic ratios in the synthesized powders were very close to the nominal values in the precursors (Table 1). Thus, the Fe/Ti atomic ratios in the synthesized powders are hereafter quoted as those in the precursors.

Valence Determination of Iron Doped in TiO_2. As will be discussed in the following sections, iron atoms are indeed doped in TiO_2. For the purposes of discussion, the valence of iron should be determined first since it plays an extremely important role in the defect structures, preferential phase formation, and magnetic properties. Nanopowders with moderate and high iron-doping concentration showed similar Mössbauer spectra. Figure 1a and b show the Mössbauer spectra collected at room temperature for the samples with $R_{Fe/Ti}$ at 5 and 20%, respectively. The spectra are fitted with a one quadrupole-split doublet: an isomer shift (IS) = 0.41 $mm{\cdot}s^{-1}$ and quadrupole splitting (QS) = 0.59 $mm{\cdot}s^{-1}$ for nanopowders with $R_{Fe/Ti}$ of 5%, and $IS = 0.38$ $mm{\cdot}s^{-1}$, $QS = 0.65$ $mm{\cdot}s^{-1}$ for nanopowders with $R_{Fe/Ti}$ of 20%. Those parameters suggest that iron doped in TiO_2 is high-spin ($S = {}^5/_2$) iron(III) ions. The Mössbauer spectra collected at 77 k are similar to those recorded at room temperature; no magnetic splitting is observed.

Phase Identification by XRD. No observable differences could be detected in the XRD patterns for powders collected on the chamber wall or filter. The configuration of the chamber wall and filter is available in the literature.[17] Therefore, the results in this work are based on the powders collected on the filter unless otherwise specified. No other phases except two modifications of TiO_2, i.e., anatase and rutile, were identified.

Figure 2a and b show the powder XRD patterns for the undoped and Fe-doped TiO_2 at $R_{Fe/Ti}$ below 5%, and 20%, respectively. For the powders with $R_{Fe/Ti} < 5\%$, the diffraction peaks are normal with a symmetric shape, whereas, in the cases of $R_{Fe/Ti} = 10$ and 20%, the diffraction peaks except for (101), (111), and (002) showed an asymmetric character. The extent of this asymmetry was remarkably enhanced with increasing $R_{Fe/Ti}$. In addition, these peaks, particularly (110), broadened and weakened. The asymmetry, broadening, and weakening of the (110) reflection with iron doping suggest a misalignment of slabs in such a way that the d spacing was not well defined in the ⟨110⟩ direction.

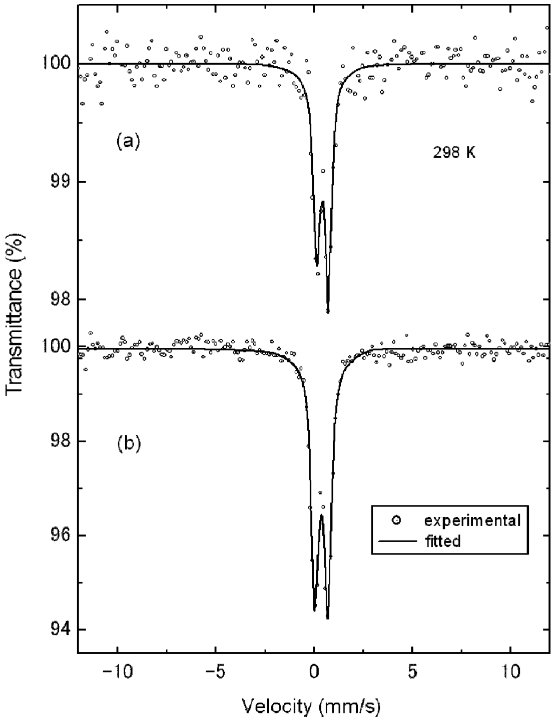

Figure 1. ^{57}Fe Mössbauer spectra of pyrogenic Fe^{3+}-doped TiO_2 nanopowders at room temperature. (a) $R_{Fe/Ti} = 5\%$; (b) $R_{Fe/Ti} = 20\%$.

No obvious preferred orientation can be identified as shown in Figure 2a. Thus, the quantitative phase composition can be determined using Chung's method, which is based on the "adiabatic principle of X-ray diffraction analysis of mixtures".[18] The intensity-concentration relationship of each component in a multicomponent system is established according to the adiabatic principle; the weight fraction of component i can be derived as

$$X_i = \left(\frac{k_i}{I_i}\sum_{i=1}^{n}\frac{I_i}{k_i}\right)^{-1} \tag{1}$$

where k_i is the intensity ratio of the strongest diffraction between the pure material i and corundum in a mixture with 1:1 weight ratio and I_i is the intensity of the strongest diffraction of component i. It can be seen in Figure 2a the strongest diffraction from anatase (101) decreases with the increase of $R_{Fe/Ti}$, while the opposite trend holds for rutile (110). The content of anatase in the synthesized TiO_2 as a function of $R_{Fe/Ti}$ is presented in Figure 3. For the undoped TiO_2, anatase percentage is approximately 78%, which is quite similar to the well-known Degussa P25 prepared by flame synthesis.[20] With iron doping, the proportion of anatase decreases rapidly with increasing $R_{Fe/Ti}$. When the $R_{Fe/Ti}$ reaches 2%, the content of rutile exceeds that

---

(20) Material data sheet for Degussa P25.

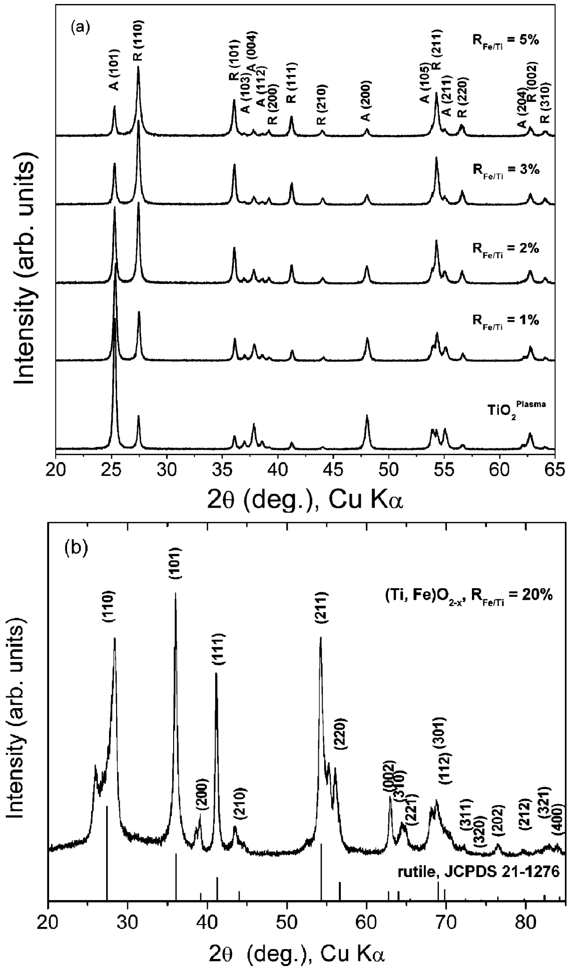

Figure 2. Powder XRD patterns for pyrogenic Fe^{3+}-doped TiO_2 nanopowders. (a) $R_{Fe/Ti}$ below 5%; (b) $R_{Fe/Ti} = 20\%$. Note asymmetric broadening and weakening of some diffraction peaks except for (101), (111), and (002). The standard XRD pattern for rutile is plotted from JCPDS file 21-1276.

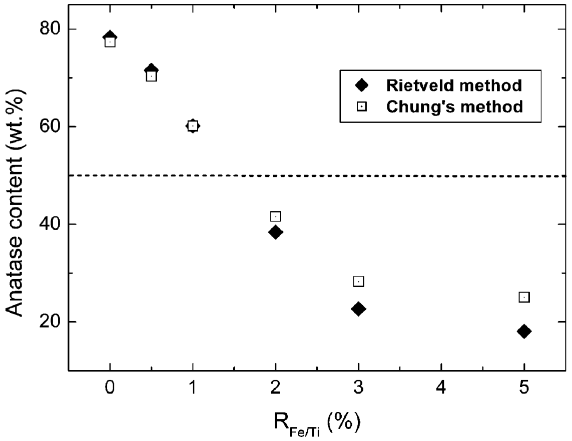

Figure 3. Anatase weight fraction of pyrogenic iron-doped TiO_2 as a function of $R_{Fe/Ti}$, iron-to-titanium atomic ratio.

of anatase as shown in Figure 3, implying that iron ions are prone to being doped in rutile.

In the quantitative calculation of phase composition based on the "adiabatic principle of X-ray diffraction analysis of mixtures",[18] the reference intensity k_i is derived from a pure material. As heteroatoms are doped, the k_i might deviate from a value based on pure phase. Therefore, the quantitative phase calculation of the iron-doped TiO_2 was also calculated with the Rietveld method using RIETAN-2000 software.[19] In the construction of crystal structures of anatase and rutile, iron ions are considered to be doped substitutionally for Ti ions. For the slightly Fe^{3+}-doped TiO_2 ($R_{Fe/Ti} \leq 1\%$), the phase fractions obtained using the two methods were similar, whereas, for the highly iron-doped TiO_2 ($R_{Fe/Ti} \geq 2\%$), the anatase fractions determined by Chung's method were somewhat larger than those determined by the Rietveld method.

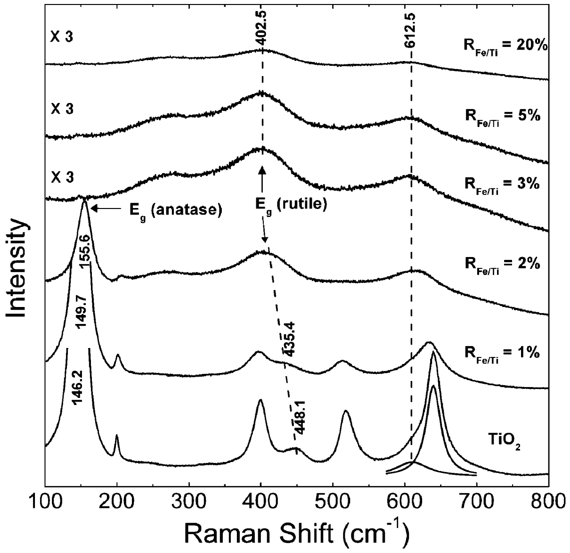

Figure 4. Raman spectra collected on undoped and iron-doped TiO_2 powders. Note the evolution of Raman bands corresponding to E_g mode for anatase and rutile with $R_{Fe/Ti}$.

Raman Spectroscopy Studies. Figure 4 shows the Raman spectra collected from the pyrogenic undoped and iron-doped TiO_2 powders. For the undoped as well as those with a low iron-doping concentration ($R_{Fe/Ti} \leq 2\%$), the characteristic Raman bands corresponding to both anatase and rutile were identified. For example, in the case of the undoped TiO_2, Raman bands at 146.2, 199.8, 399.1, 519.7 and 640.5 cm^{-1}, corresponding respectively to anatase's $E_g(\nu_6)$, $E_g(\nu_5)$, $B_{1g}(\nu_4)$, $A_{1g}(\nu_3)-B_{1g}(\nu_2)$, and $E_g(\nu_1)$ modes,[21] and 448.1 and 612.5 cm^{-1}, corresponding respectively to rutile's E_g and A_{1g} modes,[22] were observed. With increasing $R_{Fe/Ti}$, two of the six Raman bands for anatase, $E_g(\nu_6)$ and $E_g(\nu_5)$, hardened, while the rest for anatase all softened. For rutile, the Raman band of E_g mode softened until $R_{Fe/Ti}$ exceeded 2% with the increase in iron-dopant concentration, while those of A_{1g} mode likely maintained a constant value at 612.5 cm^{-1} as indicated by the dotted line in Figure 4.

When $R_{Fe/Ti}$ exceeded 2%, the Raman bands characteristic of anatase disappeared, and only those assigned to rutile can be identified. However, anatase was still present in the specimens with $R_{Fe/Ti} > 2\%$ according to XRD results (Figure 2a). This apparent disagreement is understandable in light of the fact that X-rays penetrate the bulk of particles deeper than the exciting light of the Raman spectrometer, which falls in the near-infrared region. So, Raman spectroscopy is therefore more surface-sensitive than XRD.[23] There are two possibilities that account for the disappearance of Raman bands for anatase in

---

(21) Ohsaka, T.; Izumi, F.; Fujiki, Y. *J. Raman Spectrosc.* **1978**, *7*, 321−324.
(22) Porto, S. P. S.; Fleury, P. A.; Damen, T. C. *Phys. Rev.* **1967**, *154*, 522−526.
(23) Busca, G.; Ramis, G.; Amores, J. M. G.; Escribano, V. S.; Piaggio, P. *J. Chem. Soc., Faraday Trans.* **1994**, *90*, 3181−3190.

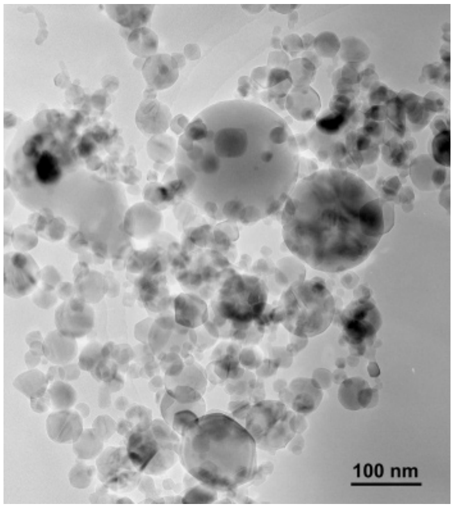

Figure 5. TEM image of undoped TiO_2, showing nanosize (20−100 nm) of approximately spherical particulates.

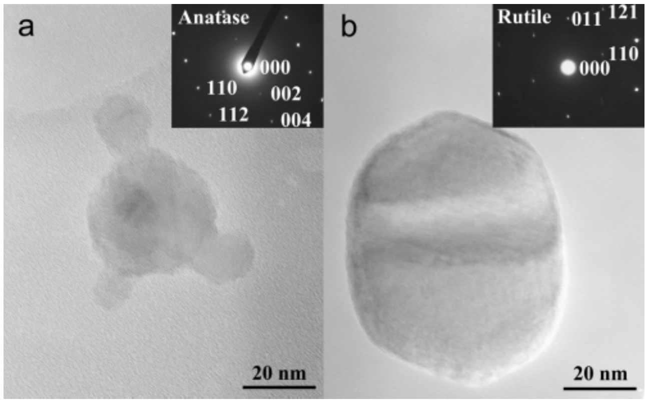

Figure 6. HRTEM images for isolated particulates of (a) anatase and (b) rutile with $R_{Fe/Ti} = 5\%$. Insets present their corresponding electron diffraction patterns.

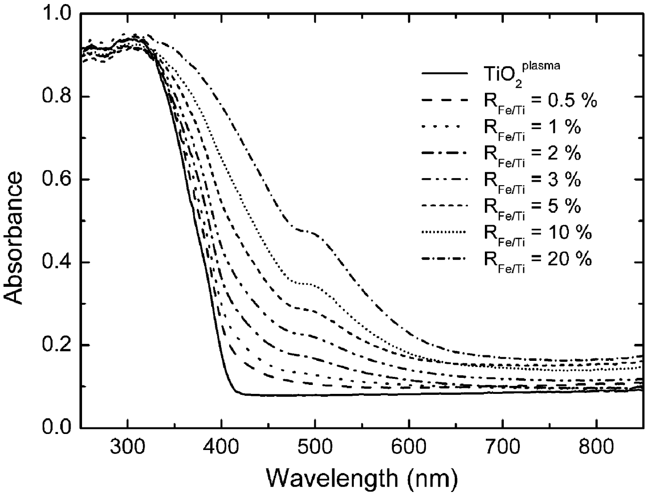

Figure 7. UV−vis diffuse reflectance spectra. Note red shift of absorption edges with iron doping and broad absorption peaks at frequencies below that of absorption cut-off.

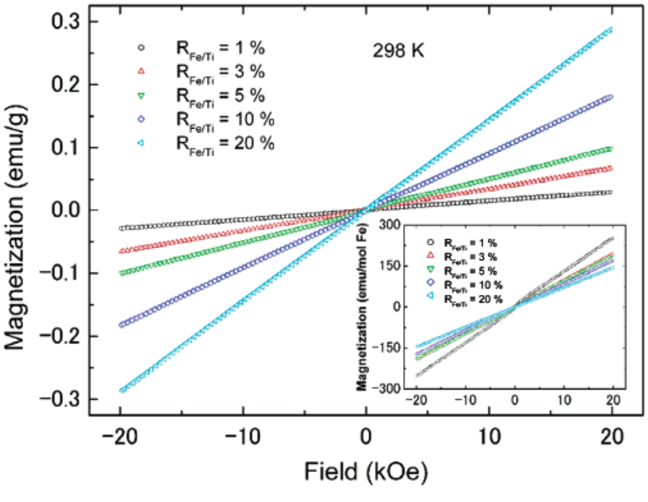

Figure 8. Magnetic field dependence of magnetization (emu per gram) at room temperature for iron-doped TiO_2 with various $R_{Fe/Ti}$ ranging from 1 to 20%. Inset shows plots of magnetization (emu per molar Fe) versus applied field.

the powder specimens with $R_{Fe/Ti} > 2\%$: an anatase@rutile core−shelled structure may have formed, or the disorder of atomic configuration in the near-surface region of anatase particulates may have been too profound to be detected by Raman spectrometer. The first possibility was ruled out after careful HRTEM examinations on isolated particulates, which is described in detail in the following section. A striking characteristic of the Raman spectra was that the intensity of Raman bands decreases remarkably with the increase of $R_{Fe/Ti}$. The phenomenon of a decrease in the intensity of the Raman bands for TiO_2 support has already been reported in V_2O_5−TiO_2 using a visible laser and was attributed to the increased absorbance of the exciting light by the sample.[24] The present data indicate that this phenomenon is a more general one, and it is reasonable to suggest that this effect is, at least in part, associated with the increased disorder on the surface of TiO_2 due to the iron ions doping.

TEM/HRTEM. Figure 5 shows a representative TEM image of the undoped TiO_2 powders. It can be seen that the particulates with approximately spherical shape are nanosized (20−100 nm). As described above, one possibility for the disappearance of Raman bands assigned to anatase when the $R_{Fe/Ti}$ exceeds 2% is that the core−shelled structure was formed. However, close HRTEM observation in combination with selected-area electron diffraction on isolated particulates demonstrates that they are either anatase or rutile, which precludes the possibility that a core−shelled structure is formed. Figure 6a and b show HRTEM images of isolated particulates corresponding to anatase and rutile at $R_{Fe/Ti} = 5\%$, respectively.

UV−vis Diffuse Reflectance Spectra. Figure 7 presents the UV−vis spectra of the resultant pyrogenic TiO_2 nanopowders. They have two principal features: (i) above a certain energy or frequency known as the absorption edge, intense absorption occurs, and the absorption edge shifts to the visible light region upon iron doping in TiO_2, and (ii) broad absorption peaks or bands appear at frequencies below that of the absorption cutoff.

Magnetic Property. Figure 8 shows the magnetic-field dependence of magnetization for iron(III)-doped TiO_2 at $R_{Fe/Ti}$ ranging from 1 to 20% at room temperature. It can be seen that magnetic susceptibility of the iron(III)-doped TiO_2 nanopowders increases with an increase in iron-doping concentration. To show how the moment may depend on Fe content, magnetization curves are also plotted in the form of magnetization (emu/mol

---

(24) Amores, J. M. G.; Escribano, V. S.; Busca, G.; Lorenzelli, V. *J. Mater. Chem.* **1994**, *4*, 965−971.

Fe) vs applied magnetic field, as shown in the inset of Figure 8. The decrease in magnetization (emu/mol Fe) with increasing iron content suggests that the magnetic moment per iron atom is decreased with an increase in iron content. Linear dependence of magnetization on magnetic field and the absence of a magnetic hysteresis loop indicate that the as-prepared iron-doped titania nanopowders are paramagnetic in nature at room temperature. The results of measuring the magnetic properties are consistent with the Mössbauer spectra (Figure 1) which show no evidence for magnetic splitting.

Discussion

Preferential Phase Formation of Anatase. Titanium dioxide crystallizes in three major different structures: rutile (tetragonal, $P4_2/mnm$), brookite (orthorhombic, $Pbca$), and anatase (tetragonal, I_1/amd). Since brookite was absent in the synthesized nanopowders, only rutile and anatase are compared here. Rutile is the most thermodynamically stable phase over a wide range of temperatures according to the thermodynamics data.[25] However, our experimental results showed that anatase rather than rutile was the major phase in the undoped TiO$_2$ powders. In the plasma-assisted synthesis procedure reported here, the cooling rate for the TiO$_2$ particles was very high ($\sim 10^6$ K/s), which is far from an equilibrium state. Therefore, the preferential formation of metastable anatase might be explained from a kinetic point of view on the basis of nucleation rate. According to classical homogeneous nucleation theory, the rate of nucleation, I, in a supercooled melt is exponentially associated with the critical nucleation energy (ΔG^*):[26]

$$I = A \exp(-\Delta G^*/kT) \tag{2}$$

where A is a pre-exponential factor related to the frequency of atom transport across the liquid−crystal interface, k is the Boltzmann constant, and T is the solidification temperature in Kelvin. For a spherically shaped nucleus, the critical nucleation energy is determined as

$$\Delta G^* = \frac{16}{3}\pi(\gamma^{\mathrm{L/S}})^3/(\Delta G_{\mathrm{V}}^{\mathrm{L/S}})^2 \tag{3}$$

where $\gamma^{\mathrm{L/S}}$ is the interfacial energy between a liquid and solid, and $\Delta G_{\mathrm{V}}^{\mathrm{L/S}}$ is the difference in Gibbs free energy per unit volume of the liquid and solid phases, which is also regarded as the thermodynamic driving force for the phase transformation, determined by the degree of undercooling of the melt.

The Gibbs free energies are available, but the interfacial energies between the liquid and solid phases of TiO$_2$ are not reported in the literature. However, the interfacial energies ($\gamma^{\mathrm{L/S}}$) can be estimated based on the theory developed by Skapski[27] using an elementary nearest-neighbors approach as

$$\gamma^{\mathrm{L/S}} = \frac{Z_i - Z_\mathrm{a}}{Z_i}\frac{\Delta H_\mathrm{m}}{N^{1/3}V_\mathrm{S}^{2/3}} + \frac{2}{3}\frac{\Delta V}{V_\mathrm{S}}\sigma + \frac{T_\mathrm{m}}{A_\mathrm{S}}(\Delta S_\mathrm{L} - \Delta S_\mathrm{S}) \tag{4}$$

where Z_i is the number of the nearest neighbors surrounding an atom in the interior of a crystal or liquid phase, Z_a is the number of neighbors of an atom at the surface of the nucleated crystal phase, ΔH_m is the molar latent heat of fusion, N is the Avogadro constant, V_S is the molar volume of the crystal phase, $\Delta V/V_\mathrm{S}$ is the relative change in volume at melting point, σ is the surface tension of the liquid at the nucleation temperature, T_m is the melting point, A_S is the molar area of the solid phases, and ΔS_L and ΔS_S are the entropy surpluses at the surface of liquid and crystal. The third term in eq 4 is always neglected in calculations as its contribution to the interfacial value is negligible.

Table 2. . Values Used for Estimation of Interfacial Energies between Liquid TiO$_2$ and Anatase and Rutile

parameters	anatase	rutile
Z_i	8	10
Z_a	4	6
ΔH_m (kJ/mol)	42.5	66.9
V_L (cm^3/mol)	21.9	
V_S (cm^3/mol)	21.4	19.8
σ (N/m)	0.38	
$\gamma^{\mathrm{L/S}}$ (N/m)	0.331	0.459

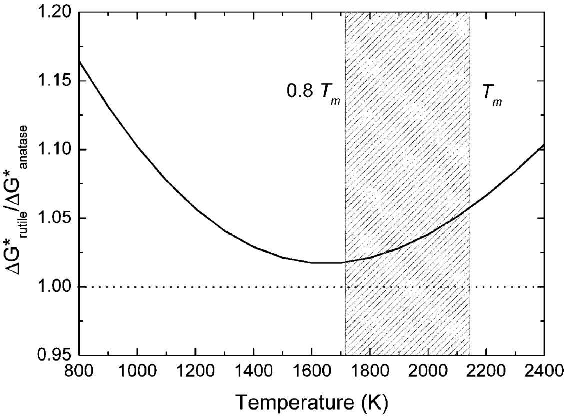

Figure 9. Temperature dependence of critical nucleation energy ratios, $\Delta G^*_{\mathrm{rutile}}/\Delta G^*_{\mathrm{anatase}}$.

Z_i and Z_a for anatase and rutile can be obtained by examining their crystal structures. Both anatase and rutile are crystallized in tetrahedral structures, but the configuration of the atoms is different. In anatase, there are four nearest neighbors to the Ti atoms and four second nearest ones, giving a total of 8 near neighbors. Therefore, Z_i for anatase is 8. The most closed plane in rutile is (110). Four atoms stand out of this plane among the 10 near neighbors in rutile crystal, so Z_a for rutile is 6. Z_a for anatase and Z_i for rutile were obtained after Li et al.[28] Other values relating to the calculation of the interfacial energies can be found in the literatures[29] and are summarized in Table 2. It should be noted that the latent heat of fusion for anatase is less than that for rutile because the phase transformation of TiO$_2$ from anatase to rutile is exothermic.

According to eq 2, the higher the critical nucleation energy, the slower the nucleation rate. Therefore, it is convenient to compare their nucleation rates by comparing the ratio of their critical nucleation energies, $\Delta G^*_{\mathrm{rutile}}/\Delta G^*_{\mathrm{anatase}}$. Figure 9 shows the temperature dependence of $\Delta G^*_{\mathrm{rutile}}/\Delta G^*_{\mathrm{anatase}}$. It can be seen that the value of $\Delta G^*_{\mathrm{rutile}}/\Delta G^*_{\mathrm{anatase}}$ is greater than unity over a wide range of temperatures. According to Skapski's result based on the theory of next-neighbors, the maximum under-

---

(25) Barin, I.; Knacke, O. *Thermochemical Properties of Inorganic Substances*; Springer: Berlin, Germany, 1973.

(26) Turnbull, D. *J. Appl. Phys.* **1950**, *21*, 1022−1028.

(27) Skapski, A. S. *Acta Metall.* **1956**, *4*, 576−582.

(28) Li, Y. L.; Ishigaki, T. *J. Cryst. Growth* **2002**, *242*, 511−516.

(29) (a) Kim, D. W.; Enomoto, N.; Nakagawa, Z.; Kawamura, K. *J. Am. Ceram. Soc.* **1996**, *79*, 1095−1099. (b) Dingwell, D. B. *J. Am. Ceram. Soc.* **1991**, *74*, 2718−2719. (c) Ikemiya, N.; Umenoto, J.; Hara, S.; Ogino, K. *ISIJ Int.* **1993**, *33*, 156−165.

cooling equals to 0.81 T_m,[30] which demonstrates that homogeneous nucleation can take place at temperatures ranging from 0.81 T_m to the melting point, T_m. As shown in Figure 9, the value of $\Delta G^*_{rutile}/\Delta G^*_{anatase}$ is greater than 1 at a range of nucleation temperatures from 0.81 T_m to T_m, indicating that metastable anatase TiO_2 nucleates preferentially in that temperature range. So anatase predominated in the pyrogenic undoped TiO_2 nanopowders.

Effect of Iron Doping on the Phase Formation of Anatase and Rutile. Doping of TiO_2 with heteroatoms introduces defects. The defects generally encountered in TiO_2 are oxygen vacancies, interstitial or substitutional Ti^{3+} ions, interstitial Ti^{4+} ions and cation vacancies. Iron doping in TiO_2 gives rise to the remarkable increase in rutile content (Figure 3), suggesting that iron is prone to being doped in rutile. The tolerance of anatase and rutile for the presence of such defects can be qualitatively correlated with the local environment of titanium in anatase and rutile. In both structures, Ti is 6-fold-coordinated, but the number of shared octahedral edges increases from two in rutile to four in anatase (Supporting Information S1 and S2). Traditional crystal chemical theory argues that shared edges should lead to cation−cation repulsion and structural destabilization, in accordance with the relative stability of both phases. As trivalent iron ions (Fe^{3+}) are substitutionally doped in TiO_2, oxygen vacancies and/or interstitial cations (Fe^{3+}, Ti^{3+}, and Ti^{4+}) would be spontaneously introduced to maintain charge neutrality. Because oxygen vacancies or interstitial cations carry a positive charge, iron ions are therefore prone to being doped in rutile, which has greater tolerance than anantase toward oxygen vacancies due to fewer shared edges in the crystal structure of rutile. TiO_2 doped with other trivalent ions such as Al^{3+} showed similar preferential formation of rutile over anatase.[31] In contrast, if the ions have valences greater than four, as Ti^{4+} in TiO_2, cation vacancies should form. It is suggested that the presence of such cation vacancy can be better tolerated in an anatase structure due to the better charge defect compensation by the neighboring Ti cations.[32]

Near-Surface Defect Structure. Because Raman spectroscopy is more surface-sensitive than X-ray diffraction, it can be used to investigate near-surface defect structures. Parker and Siegel[33] systematically investigated nanophase TiO_2 using Raman spectroscopy. They found that the Raman bands corresponding to the E_g modes in both anatase and rutile were sensitive to oxygen deficiency, and the peak position of the E_g mode (143 cm^{-1}) for anatase blue-shifted while that (447 cm^{-1}) for rutile red-shifted with the increase in oxygen defect. This finding presented potential quantitative indicators of these deviations from stoichiometry. In our present work, the peak position of the E_g mode for anatase blue-shifted and that for rutile red-shifted with an increase in the iron-doping concentration (Figure 4). With Fe^{3+} doping in TiO_2, oxygen vacancies would arise to maintain charge equilibrium. The concentration of oxygen defects should increase spontaneously with the increase in the iron ions doped in TiO_2, accompanying a consequent shift in the peak position of the Raman bands. Since the peak position of the Raman bands corresponding to anatase and rutile shift with the same tendency as caused by oxygen deficiency in nanophase TiO_2,[33] it is reasonable to conclude that these shifts of the Raman bands are attributed to oxygen deficiency resulting from iron doping of TiO_2. In addition, the peak position of the E_g mode (143 cm^{-1}) for anatase was observed to blue-shift, while that (447 cm^{-1}) for rutile red-shifted in TiO_2 powders obtained from $Ar-O_2$ plasma oxidation of TiC powders with decreasing oxygen flow rates.[34]

The lattice vibrations at $k = 0$ for rutile TiO_2 show that the E_g mode (447 cm^{-1}) is due to the out-of-phase vibrational motion of the oxygen atoms along the *c*-axis.[35,36] This mode is nonpolar and independent of the directional approach to $k = 0$, and as pointed out by Maroni,[36] the planar O−O interactions are more important to the lattice dynamics of rutile than the Ti−O stretching. As a result, the absence of oxygen in these planes would have a more significant effect on E_g mode (447 cm^{-1}) than, for example, the Ti−O stretching mode (A_{1g}) at 612 cm^{-1}. This is also the case for the iron-doped TiO_2 in the present work; the peak position of the E_g mode for rutile red-shifted, whereas there was almost no influence on the A_{1g} mode (612 cm^{-1}) with increasing the iron-doping concentration. This result further supports that the shift of Raman bands are due to oxygen deficiency created by the substitution of Fe^{3+} for tetravalent Ti^{4+} in TiO_2.

As described above, no other phases except two modifications of TiO_2, anatase and rutile, are identified using XRD and Raman spectroscopy, suggesting that iron ions are doped in TiO_2. Therefore, the oxygen deficiency seems to increase with the increase in the concentration of iron dopant. However, it is interesting to find that with a higher iron-doping concentration ($R_{Fe/Ti} > 2\%$), the peak position of Raman bands remains almost constant, which suggests that the oxygen deficiency contributing to the shift in the Raman bands is saturated. In other words, the oxygen deficiency tends to concentrate, resulting in the formation of an extended defect like a crystallographic shear structure. This well-recognized phenomenon is discussed in the following section.

Crystallographic Shear Structure in Highly Iron-Doped TiO_2. For a long time it has been known that certain transition metal oxides could be prepared with an apparently wide range of nonstoichiometry, e.g., WO_{3-x}, MoO_{3-x}, TiO_{2-x}. Following the work of Magneli, it was recognized that, in these systems, instead of continuous solid solution formation, a series of closely related phases with very similar formulas and structures existed.[37] As discussed above, the concentration of oxygen vacancies increased to its maximum as $R_{Fe/Ti}$ reached 2%. It seems likely that any further oxygen defects that formed would tend to aggregate at random or in an ordered form. The X-ray diffraction results showed that some diffractions broadened asymmetrically, while (101), (111), and (002) did not, indicating that the defects probably aggregated in an ordered form. The crystallographic shear structure is an ordered defect type in nonstoichiometric TiO_{2-x}, MoO_{3-x}, and WO_{3-x}.[38] It is charac-

---

(30) Skapski, A. S. *Acta Metall.* **1956**, *4*, 583−585.
(31) (a) Vemury, S.; Pratsinis, S. E. *J. Am. Ceram. Soc.* **1995**, *78*, 2984−2992. (b) Kim, S.; Gislason, J. J.; Morton, R. W.; Pan, X. Q.; Sun, H. P.; Laine, R. M. *Chem. Mater.* **2004**, *16*, 2336−2343.
(32) Arbiol, J.; Cerda, J.; Dezanneau, G.; Cirera, A.; Peiro, F.; Cornet, A.; Morante, J. R. *J. App. Phys.* **2002**, *92*, 853−861.
(33) (a) Parker, J. C.; Siegel, R. W. *Appl. Phys. Lett.* **1990**, *57*, 943. (b) Parker, J. C.; Siegel, R. W. *J. Mater. Res.* **1990**, *5*, 1246−1252.
(34) Li, Y. L.; Ishigaki, T. *J. Phys. Chem. B* **2004**, *108*, 15536−15542.
(35) Trayler, J. G.; Smith, H. G.; Nicklow, R. M.; Wilkinson, M. K. *Phys. Rev. B* **1971**, *3*, 3457−3472.
(36) Maroni, V. A. *J. Phys. Chem. Solids.* **1988**, *49*, 307−313.
(37) West, A. R. *Basic Solid State Chemistry*; John Wiley & Sons: Chichester, 1999.
(38) Bursill, L. A.; Smith, D. J. *Nature* **1984**, *309*, 319−321.

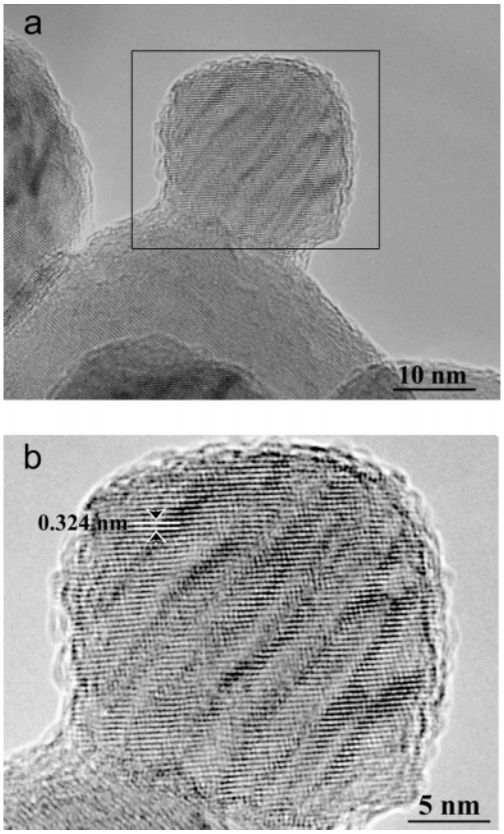

Figure 10. HRTEM images of iron-doped nanopowder with $R_{Fe/Ti} = 20\%$. (a) General morphology; (b) magnification of rectangle region in (a). *d* spacing of 0.324 nm corresponds to rutile {110} planes.

terized by regions of normal structure in stoichiometric oxides separated from each other by crystallographic shear planes (CS planes) which are thin lamellae of rather different structure and composition. Almost all of the oxygen deficiencies are concentrated within these CS planes. In the work presented here, CS planes were observed in the iron-doped TiO_2. A few thin lamellae of CS planes were observed in the slightly iron-doped nanopowders, and the number of the lamellae increased with the increase in the iron-dopant concentration. Figure 10 shows typical lattice images of iron-doped nanopowder at $R_{Fe/Ti} = 20\%$. These clearly show that normally the rutile structure is separated by approximately parallel lamellae of CS planes. In a normal rutile structure, there are only corner- or edge-sharing octahedra, while face-sharing octahedra exist in the CS planes,[39] which led to misalignment of the slabs in such a way that the *d* spacing, like (110), is not well-defined in the ⟨110⟩ direction. As a result, the (110) reflection broadened abnormally (Figure 2b).

UV−vis Diffuse Reflectance Spectra. Estimations of the band-gap energies were obtained from the diffuse reflectance spectra of the pyrogenic undoped and iron-doped powders. Semiconductors are classified as either direct or indirect according to the lowest allowed electronic transition. Direct semiconductors are characterized by the minimum of the lowest conduction band positioned in *k* space directly under the maximum of the highest valence band. For indirect semiconductors, the minimum of the lowest conduction band being shifted relative to the maximum of the highest valence band, and the lowest-energy interband transition must then be accompanied by phonon excitation.[40] Both direct and indirect interband transitions occur simultaneously under irradiation with sufficient energy. Those two different kinds of transitions can be distinguished by their energy dependence of the optical absorption edge. The relation between the absorption coefficient (α) and incident photon energy ($h\nu$) can be written as $\alpha = B_d(h\nu - E_g)^{1/2}/h\nu$ and $\alpha = B_i(h\nu - E_g)^2/h\nu$ for allowed direct and indirect transitions, respectively, where B_d and B_i are absorption constants for direct and indirect transitions, respectively.[41]

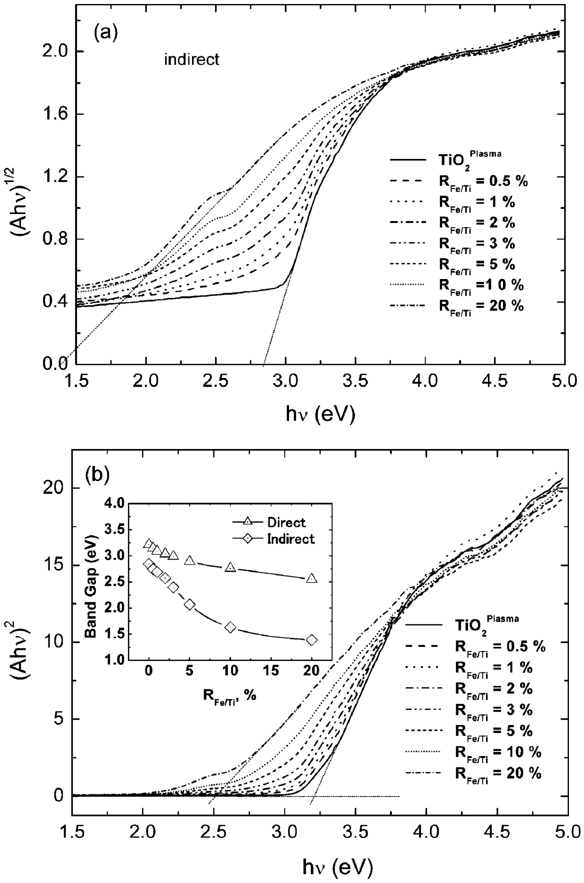

Figure 11. (a) Plots of $(Ah\nu)^{1/2}$ versus $h\nu$; (b) plots of $(Ah\nu)^2$ versus $h\nu$. Inset shows dependence of direct and indirect transition energies on iron-doping level in TiO_2. "A" in the *Y* axis title represents absorbance, which is proportional to absorption coefficient (α).

Plots of $(Ah\nu)^{1/2}$ versus $h\nu$ from the spectral data in Figure 7 are presented in Figure 11a. Extrapolating the linear part of the curve for the undoped TiO_2 gives an indirect band gap of 2.84 eV, which is very close to the calculated value of 2.91 eV corresponding to $X_{1a} \rightarrow G_{1b}$ indirect interband transition.[42] With iron doping, the linear parts of the curves become indefinite. In contrast, good linear relationships are obtained when the curves are plotted as $(Ah\nu)^2$ versus $h\nu$. Thus, the stronger absorption features in Figure 11b are those of the allowed direct band transitions. For the undoped TiO_2, extrapolating the linear part of the curve gives a direct transition of 3.22 eV, which is very close to 3.3 eV for the experimental bulk crystal[43] and the

---

(39) Bursill, L. A.; Blanchin, M. G.; Smith, D. J. *Philos. Mag. A* **1984**, *50*, 453−472.

(40) Serpone, N.; Lawless, D.; Khairutdinov, R. *J. Phys. Chem.* **1995**, *99*, 16646−16654.

(41) (a) Mooser, E.; Pearson, W. B. In *Progress in Semiconductors*; Gibson, A. F. Ed.; John Wiley & Sons: New York, 1960; Vol. 5, p 53. (b) Zhao, X. K.; Fendler, J. H. *J. Phys. Chem.* **1991**, *95*, 3716−3723.

(42) Daude, N.; Gout, C.; Jouanin, C. *Phys. Rev. B* **1977**, *15*, 3229−3235.

(43) Frova, A.; Body, P. J.; Chen, Y. S. *Phys. Rev.* **1967**, *157*, 700−708.

calculated value of 3.45 eV corresponding to X_{1a}→C_{1b} direct interband transition.[41] Analogous to the tendency for indirect transitions, the direct transition energies were also reduced with increasing the iron-dopant concentration, as shown in the inset in Figure 11b. The reduction in the energies for both indirect and direct transitions with iron doping is ascribed to the introduction of Fe^{3+} 3d states in the conduction band of TiO_2.

In addition, a striking feature in the UV−vis diffuse reflectance spectra (Figure 7) is the appearance of broad absorption peaks or bands at frequencies below that of the absorption cutoff. These absorption bands are generally associated with one type of transitions, i.e., the promotion of an electron from a localized orbital on one atom to a higher-energy localized orbital on the same atom.[37] In the present case, the absorption is associated with d−d electron transition of iron atoms.

Magnetic Properties. According to our measurements of the magnetic properties, as well as the Mössbauer spectra of the iron-doped TiO_2 nanopowders at room temperature, it is reasonable to conclude that they are paramagnetic even with an iron-dopant concentration as high as 20% ($R_{Fe/Ti}$). These results suggest the absence of magnetic ordering in the iron-doped TiO_2 at room temperature. No iron clusters were formed due to the high oxygen pressure, which was confirmed by careful HRTEM examination. Therefore, at this point, it is plausible to conclude that the iron-doped TiO_2 nanopowders are paramagnetic in nature. This is not difficult to understand in view of the fact that ferromagnetic Co-doped TiO_2 films and/or powders are invariably prepared in a high vacuum[9−12] or postannealed in conditions with low oxidation pressure[44] in which metallic Co clusters have a greater tendency to form, while those prepared under high oxygen pressure are paramagnetic. Our results support those of recently published studies[14,44] which reported that the ferromagnetic nature of Co-doped TiO_2 (anatase and/or rutile) in the forms of films or powders results from magnetic cobalt metal clusters. Based on the Mössbauer spectra collected at 77 k, the absence of magnetic splitting for the iron-doped TiO_2 suggests that they are not ferromagnetic even at that low temperature.

Conclusions

Under extreme synthesis conditions, undoped and iron(III)-doped TiO_2 nanopowders with controlled $R_{Fe/Ti}$ up to 20% were fabricated using oxidative pyrolysis in RF thermal plasma. In the undoped TiO_2 nanopowders, metastable anatase predominated in the resultant nanopowders consisting of anatase and rutile, which was explained from a kinetic point of view based on classical nucleation theory. Iron doping greatly promoted the formation of rutile because of its higher tolerance to defects such as oxygen vacancies resulting from the substitution of Fe^{3+} for Ti^{4+} in TiO_2. Meanwhile, the concentration of oxygen vacancies reached a maximum at $R_{Fe/Ti} = 2\%$, above which surplus oxygen vacancies tended to concentrate into an extended defect structure like a crystallographic shear (CS) plane. Iron doping in TiO_2 led to a narrowing of the band gap. The paramagnetic nature of the as-prepared iron-doped TiO_2 nanopowders at room temperature was determined by magnetic property measurements and Mössbauer spectra.

Acknowledgment. We thank Dr. C. Y. You for the helpful discussion on the magnetic properties. This work was partly supported by Industrial Technology Grant Program, Contract Number ID04A26018, from New Energy and Industrial Technology Development Organization (NEDO), Japan.

Supporting Information Available: Crystal structural models of rutile and anatase, showing the difference in shared octahedral edges (PDF). This material is available free of charge via the Internet at http://pubs.acs.org.

JA051240N

---

(44) Cho, J. H.; Kim, B. Y.; Kim, H. D.; Woo, S. I.; Moon, S. H.; Kim, J. P.; Cho, C. R.; Joh, Y. G.; Kim, E. C.; Kim, D. H. *Phys. Status Solidi B* **2004**, *241*, 1537−1540.